Interface matters: Design of an efficient $CaCu_3Ti_4O_{12}$-rGO photocatalyst

F.M. Praxedes [a], H. Moreno [a,*], A.Z. Simões [a], V.C. Teixeira [b], R.S. Nunes [a], R.A.C. Amoresi [a], M.A. Ramirez [a]

[a] São Paulo State University – UNESP, Faculty of Engineering of Guaratinguetá, Av. Dr. Ariberto Pereira da Cunha 333, Portal das Colinas, Guaratinguetá, São Paulo, Brazil
[b] Brazilian Synchrotron Light Laboratory (LNLS), Brazilian Center for Research in Energy and Materials (CNPEM), 13083-970 Campinas, SP, Brazil

ARTICLE INFO

ABSTRACT

Different strategies have been investigated to enhance optical properties of semiconductor oxides such as $CaCu_3Ti_4O_{12}$, e.g., reduced graphene oxide. This research focuses on photoluminescent and photocatalytic properties of $CaCu_3Ti_4O_{12}$-rGO composites. Micrometric CCTO and rGO particles were mixed to obtain composites. (Micro)structure, photoluminescence, and photocatalytic properties were evaluated. CCTO-rGO composites displayed broad PL emission over the visible spectrum, useful for triggering photocatalytic applications ($\approx$ 380–750 nm). A shift in PL towards the violet region compared to pure CCTO along with an associated orange emission decrease may be ascribed to rGO activity as an electron donor/acceptor. Photocatalytic tests under UV light (325 nm) showed that 20%rGO ($\approx$ 25.88%) significantly improved rhodamine B removal/adsorption compared to pure CCTO ($\approx$ 9.64%). Results from this study show that CCTO-rGO composites may be a promising choice for future UV–visible light-driven photocatalytic devices with high adsorption/lower response time promoting sustainability in water purification methods and associated applications.

© 2022 Elsevier B.V. All rights reserved.

1. Introduction

Functional materials studies have advanced over the recent decades, resulting in overall improved performance and expanded applications. Calcium copper titanate (CCTO) falls into this category. A pseudo-perovskite of the type AA'BO₃ with space group *Im-3*, in which the Cu^{2+} and Ca^{2+} ions share the A sites [1], CCTO-based ceramics first attracted the attention of scientists around the globe for behaving as a nonohmic material ($\alpha \sim 55$) [2,3]. Moreover, CCTO exhibits a giant dielectric permittivity ($\varepsilon \sim 10^4$–10^5) over wide frequency (10^{-2}–10^6 Hz) and temperature (100–600 K) ranges [4–6], which enables its application as varistors [2,3] and capacitors [7,8], respectively. These materials are also suitable for energy production [9], light-emitting diodes [10], photovoltaic panels [11,12], water treatment (e.g., adsorbents [13,14], and catalysts [15–20], whose photoluminescent (PL) and photocatalytic (PC) properties play a key role. TiO₂ has been extensively studied for such applications, however, its photocatalytic efficiency is significantly affected by electron-hole pair recombination [21]. As an alternative, researchers have applied complex metal oxides, in which defects within the optical bandgap region lead to optimized charge transference between particles [22].

Enhancing solar energy harnessing for solving the global energy crisis and for environmental solution has brought forth many technologies. Materials scientists have developed different techniques to improve visible-light-driven photocatalyst efficiency, including composite synthesis to form heterojunctions (e.g., chitosan fibers/Ag-Ag₃PO₄, carbon fiber/n-TiO₂/p-Ag₂O junctions) [23,24], morphology control on PC particles [25–27]. In this sense, CCTO-based ceramics ($E_{gap} \sim 2.3$ eV) characterized by the presence of oxygen vacancies as a result of Ti^{4+} and Cu^{2+} reduction into Ti^{3+} and Cu^+ respectively, may be attractive for PL and PC applications [28]. Moreover, CCTO are easy to synthesize on a large scale by processes such as the solid-state reaction method. Oxygen-related defect PL response depends on the presence of $[TiO_5 \cdot V_o^\bullet]$ and $[CaO_{11} \cdot V_o^\bullet]$ clusters within CCTO electronic structure in a way that emissions vary with defect depth in the bandgap: (1) violet-blue emissions can be associated with shallow defects; (2) yellow-green with electron-hole pair recombination; and (3) orange-red emissions may be related to deep-level defects [28]. Researchers have explored different possibilities in order to improve PL response synthesizing $CaCu_3Ti_4O_{12}/CaTiO_3$ ceramic composites [29], and doping CCTO with different metals (e.g., Sr and W) [30,31]. Photocatalytic response in CCTO ceramics may be originated by the hybridization of Cu(3d) and O(2p) orbitals and enhanced by electron-hole pair recombination effects, improving oxidation processes [32]. This behavior has fostered studies regarding the PC response of CCTO-based ceramics [33–35].

Recently, carbonaceous compounds (e.g., carbon nanotubes, graphene, etc.) proved to be an alternative to enable high transferability

* Corresponding author.
E-mail address: hpiccolimoreno@gmail.com (H. Moreno).

rates of photogenerated electrons within its electronic structure acting as electron acceptors due to their high electrical conductivity. Graphene oxide (GO) and reduced graphene oxide (rGO) have a very similar structure to graphene, which is formed by sp^2 hybrid bonds. However, oxidation processes during synthesis create high defect density structure evidenced by the presence of oxygenated functional groups [36–40]. Studies show that electrons can react with these functional groups forming free radicals [41–43]. Functional groups act as photosensitizers which, in addition to rGO high surface area, enhance PC response [43]. Recently, many studies have investigated rGO influence on the photoluminescence of different compounds (e.g., TiO_2, $CsPbBr_3$, V_2O_5, etc.) [43–45]. Researchers have also studied the influence of rGO on composites applied to photocatalysis (e.g., $La_2Zr_2O_7$, $BiFeO_3$, and Fe_3O_4) [15,46,47]. The authors reported significant improvement of PC activity towards NO_x [48], antibiotic [49–51], and dye [52–55] degradation. Rhodamine B (RhB) is one of the most widely studied dyes due to its use in varied industry applications as well as for its reduced level of environmental and health risks. [56,57].

At the time of writing this paper, and to authors' best knowledge, there are no reports on the dependence of PL and PC response of CCTO-rGO composites. Hence, this work combines experimental (micro)structural and optical analysis to propose a practical model explaining rGO effect on CCTO PL response, as well as PC regarding RhB degradation under UV–visible light. The results show CCTO-rGO composites may be a promising choice for future UV–visible light-driven photocatalytic devices with high adsorption and lower response time. Additionally, the possibility to trigger photocatalysis by sunlight makes it an important step towards achieving sustainability in water purification methods, etc.

2. Materials and methods

2.1. rGO synthesis

rGO synthesis was performed using the modified Hummers method based on the methodology proposed by Abdolhosseinzadeh [54]. In the oxidation stage, graphite (5 g) was added to 50 mL H_2SO_4 under constant temperature (ice bath <10 °C) with stirring. Then, potassium permanganate (6 g) ($KMnO_4$, was slowly added to the (graphite + H_2SO_4) mixture, which remained under constant stirring for 20 min. This mixture (graphite + H_2SO_4 + $KMnO_4$) was submitted to an ultrasonic bath for 10 min. This process (stirring – ultrasonic bath) was repeated 12 times. Following the oxidation process, deionized water (500 mL) was added under constant temperature (<10 °C) and stirring. The mixture was exfoliated in an ultrasonic bath for 2 h, and the system (solution + GO) was washed several times until pH ≈ 6. To reduce GO, distilled water (500 mL) was added, and the mixture was stirred for 1 h in an ultrasonic bath. Then, ascorbic acid solution (500 mL) ($C_6H_8O_6$, Synth, 20%) was added under constant stirring for 1 h. Finally, the system was heated to 90 °C ± 5 °C and stirred for 1 h, the solution was filtrated, and washed. The collected powder was dried at 85 °C for 12 h to obtain rGO.

2.2. Synthesis of CCTO powders

In the synthesis of CCTO powders via solid-state reaction, $CaCO_3$ (Sigma-Aldrich 99.99%), CuO (Sigma-Aldrich 99.99%), and TiO_2 (Sigma-Aldrich 99.99%) were used as precursors in stoichiometric proportions. The starting reagents were weighed and mixed in an isopropyl alcohol medium in a rotary mill for 24 h. The mixture was dried at 60 °C for 12 h, sieved (200#-mesh), and calcined for 12 h at 900 °C, as previously determined by thermal analysis (Fig. S1). Finally, the samples were submitted to milling in an isopropyl alcohol medium over 12 h for eliminating neck-like junctions between particles formed during calcining. Then, the material was dried at 60 °C for 6 h and sieved (200# - mesh), ready to mix with rGO.

2.3. Synthesis of CCTO-rGO composite

The composites were obtained using a mechanical method by adding x% rGO (x = 0%, 1%, 2%, 5%, 10%, and 20 wt%) to the CCTO powders. First, the rGO powder was stirred for 5 min in 10 mL of isopropyl alcohol. Then, CCTO +40 mL of isopropyl alcohol was added to the rGO + isopropyl alcohol under constant stirring for 25 min. The mixture was milled in an isopropyl alcohol medium for 6 h in a rotary mill. Finally, the powders were dried for 6 h at 60 °C and sieved (200#-mesh). The samples were named CCTOxrGO, where "x" stands for the wt% value.

2.4. CCTO-rGO composite characterization

2.4.1. (Micro)structural characterization

The long-range structure of the composites was characterized using X-ray powder diffraction (XRPD) performed on a Bruker (model D8 Advance). The XRPD analysis was performed over a 10°-90° 2θ-range, with a step-size of 0.02°, 10 s/point collection time, and sample rotation of 10 rpm, operating at 40 kV/25 mA and using copper K_α radiation (1.5406 Å). GSAS II free software [59] was used to perform *Rietveld* analysis [60], employed to further evaluate crystal structure on the CCTO-rGO composite system. Infrared spectroscopy in the Fourier transform-infrared spectroscopy (FTIR) was performed on a spectrophotometer (model Spectrum 100, Perkin Elmer) under Attenuated Total Reflection mode to identify rGO functional groups. The FTIR spectra were recorded over the 4000–650 cm^{-1} range with a 4 cm^{-1} resolution. Raman spectroscopy was carried out using a Renishaw (inVia Qontor) Raman scattering microscope equipped with an argon-ion laser ($\lambda \approx 532$ nm). The average between three sequential scans was used to compose the final spectra, with a spectral step of ~ 1.13 cm^{-1} over the range of 350 cm^{-1} to 3500 cm^{-1}.

X-ray Absorption Near-Edge Structure (XANES) data were collected around the Ti K-edge ($E_0 \approx 4966$ eV) at the X-ray Absorption and Fluorescence Spectroscopy (XAFS1) beamline at the Brazilian Synchrotron Light Laboratory. The experiment was performed on transmission mode using thin membranes at room temperature. A Ti-foil standard was used to calibrate the monochromator, and TiO_2 and Ti_2O_3 were used as reference materials for the measurements. Three sequential scans were obtained for each sample to minimize the signal-to-noise ratio and the experimental data were analyzed using the software ATHENA [61]. Finally, particle morphology of the composite was evaluated by scanning electronic microscopy (SEM) using a Zeiss Evo LS15. Surface area, pore radius, and pore volume were determined through the Brunauer-Emmett-Teller (B.E.T.) method.

2.4.2. Optical characterization

Ultraviolet-visible absorption studies were performed at room temperature on a Cary 50 Bio in diffuse reflectance mode over the 360–830 cm^{-1} range. Bandgap energy (E_{gap}) calculations were based on the *Kubelka-Munk* equation (Eq. (1)),

$$(\alpha h\nu) = F(R)h\nu = C_1 \left(R_\alpha \left(h\nu - E_{gap} \right)^n \right) \tag{1}$$

where α is the linear absorption coefficient, h Planck's constant ($h = 4.1357 \times 10^{-15}$ eV.s^{-1}), ν the frequency of the light, C_1 is a constant, R_∞ is the reflectance when the sample is taken as infinitely thick, and E_{gap} corresponds to the gap energy of the material. Additionally, the variable $n = 2$, corresponds to direct forbidden transitions. Data acquired were used for Tauc plots in $(\alpha h\nu)^2$ vs. $(h\nu)$. Photoluminescence analysis was performed using a spectrophotometer Ocean Optics (model QE65000) to collect the emission signal and a diode laser with $\lambda_{exc} = 350$ nm (100 mW) for exciting the samples.

For the photocatalytic test, a UV lamp ($\lambda_{max} = 254$ nm, 11 W, Osram, Puritec HNS 2G7) covered by a quartz tube was placed inside a

photocatalytic reactor containing both the dye and catalyst suspensions, under constant stirring and air supply. Photocatalyst concentration used was 0.125 g L^{-1}. RhB$_{(aq)}$ solution concentration (C_0: 1×10^{-5} mol. L^{-1}, and the same concentration to the ciprofloxacin test) was measured at -20, 0, 5, 10, 15, 30, 60, 90, and 120 min (the time indicated as "-20" represents the time the sample remained in the dark to reach dye adsorption-desorption equilibrium). To measure concentration of the solution, a Perkin Elmer® Lambda 1050 spectrophotometer was used based on the Lambert-Beer law. RhB degradation kinetics was evaluated combining the pseudo-first-order (Eq. (2)) and the Langmuir–Hinshelwood equation (Eq. (3)):

$$\ln \left(\frac{C_0}{C} \right) = kt \tag{2}$$

$$t_{1/2} = \frac{\ln 2}{k} \tag{3}$$

where C_0 is the initial concentration, C the concentration at a specific time, t the irradiation time, k the pseudo-first-order rate constant, and $t_{1/2}$ the time for a 50% discoloration. To determine the main active species, photocatalytic experiments using scavengers were carried out using 2Na-EDTA (1.0 mmol L^{-1}), p-benzoquinone (1.0 mmol L^{-1}), and isopropanol (0.01 mL/mL RhB solution). Adsorption and photodiscoloration stability for the CCTO20rGO sample was analyzed along the test cycles. The photocatalyst was washed with deionized water, dried at 80 °C, and heat treated at 400 °C for 1 h after each cycle to completely remove RhB from the sample [62,63].

3. Results and discussion

3.1. rGO characterization

Fig. 1(a) shows XRPD diffractograms for rGO (red curve) and graphite (Gr, black curve), used as a starting reagent. Fig. 1(b) highlights the rGO diffraction peaks. Graphite was indexed by phase ICSD 18838 (space group *P63/mmc*) (Fig. 1a) with diffraction peaks at ~26.55°, 42.57°, 44.83°, 54.81°, 77.57°, and 83.82°. In Fig. 1(b) all peaks observed (~24.90°, 42.68°, and 78.00°) were associated with the rGO phase. Following GO chemical reduction, the sharp peak associated with the crystallographic plane (002) is replaced by a broad peak shifted towards lower 2θ values [64]. Thus, it is reasonable to assume this broad peak originates from partial restacking of the exfoliated layers in the graphene oxide structure [65]. Furthermore, a shoulder-like feature at 2θ~16° (indicated by the dashed line, Fig. 1b) may be associated with water molecules in the rGO structure [66]. Raman spectra (Fig. 1c) reveals the presence of vibrational bands D (1350 cm^{-1}) and G (1597 cm^{-1}) both in Gr and rGO. The D band can be associated with sp^2 domain defects and displacements within graphene layers, as well as at graphene edges. On the other hand, the G band is related to the stretching vibration mode E_{2g}, in the plane of hybridized atoms sp^2 [67]. I$_D$/I$_G$ ratio indicates disorder in graphitic structured materials, in a way that increasing its value suggests higher defect density in the evaluated structure [55,64,65]. Generally, the I$_D$/I$_G$ ≈ 1.08 for rGO [55,66], which is in accordance with the estimated values in this study, confirming the successful rGO synthesis. This study's results
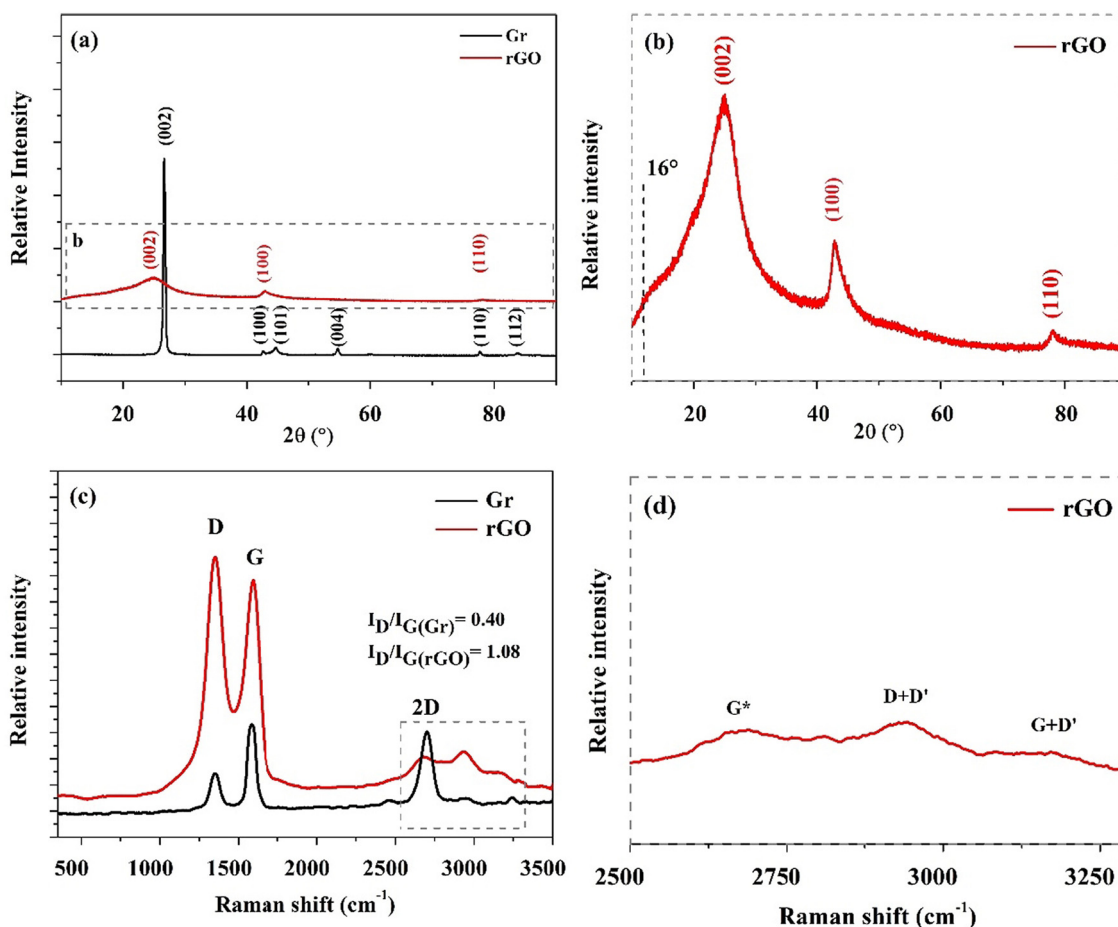

Fig. 1. (a) Diffractogram of the precursor graphite (Gr) and the rGO, (b) rGO diffractogram, (c) Raman spectra of graphite and rGO, and (d) G*, D + D′ and G + D′ bands in rGO spectra.
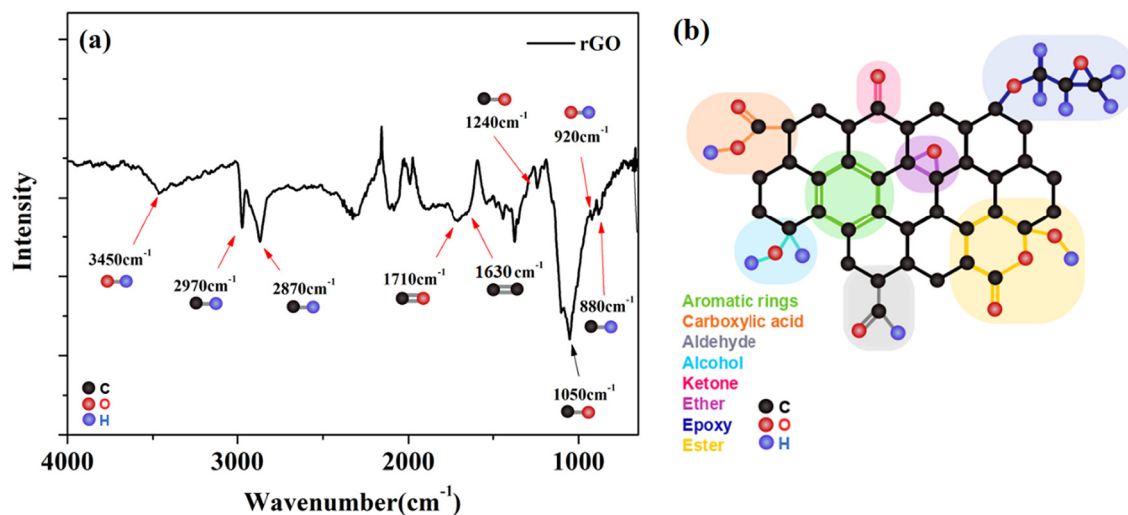
Fig. 2. (a) FTIR spectrum and (b) illustration of functional groups in an rGO structure.

indicate an evolution of D and G bands towards an I_D/I_G ratio increase due to sp^3 bond formation during the exfoliation process (*Hummers* method), generating structural defects within the rGO layers. The presence of G^*(2500 cm^{-1}), D + D′ (2900 cm^{-1}), and G + D′ (3200 cm^{-1}) bands in the rGO spectrum (Fig. 1d) can be related to the number of graphene layers and chemical processes. Monolayer graphene presents an intense 2D band at $\approx$ 2700 cm^{-1} whose intensity decreases with the addition of extra graphene layers, leading to the formation of the bands G^*, D + D′, and G + D′ [64]. 2D band suppression can also occur in structures with chemically induced defects [55,67,68]. Thus, based on the XRPD and Raman spectroscopy analyses, it is reasonable to assume that multilayer rGO was successfully synthesized using the modified *Hummers* method.

Fig. 2(a) exhibits the FTIR spectrum for the synthesized rGO using the modified Hummers method. A broadband at 3000-3600 cm^{-1} is characteristic of O–H stretching vibrations. O–H functional groups are particularly relevant regarding photocatalytic properties, since photogenerated holes may react with OH groups to form OH radicals [66]. At $\approx$ 2970 cm^{-1} and $\approx$ 2870 cm^{-1}, the vibrational bands correspond to C–H bonds. At $\approx$ 1710 cm^{-1} there is a band related to C=O stretching vibrations in the carbonyl group. Likewise, aromatic C=C vibration in the graphene planes can be identified at $\approx$ 1630 cm^{-1}, and C–O–C stretching vibration in the epoxy group at $\approx$ 1240 cm^{-1}, while at $\approx$ 1100 cm^{-1}, a C–H band in alcohol occurs; while around 1050 cm^{-1}, the band can be related to C–O stretching vibrations, and at $\approx$ 920 cm^{-1}, the band can be associated with O–H bending vibrations in carboxylic

acid. Finally, at $\approx$ 880 cm^{-1}, the band may be associated with C–H bending vibrations in the aromatic group. Therefore, the presence of vibrational bands related to C–H, C–O, C=O, and O–H bonds in the rGO FTIR spectrum suggest the existence of carboxylic acid, esters, aldehyde, and ketone functions as illustrated in Fig. 2(b), which occur mainly along the edges of an rGO sheet, and also on the basal plane of graphene sheets [69,71,72].

Fig. 3(a-b) displays SEM micrographs of Gr and rGO particles. Both Gr and rGO show micrometric particle size. In Fig. 3(b), the rGO sample exhibits a superficial modification with increased roughness. A similar morphology is reported in the literature [38], which may be associated with the low number of rGO layers [64] in the sheets are still detached from each other. This morphology can be a consequence of the defects in the graphitic structure like carbon ring distortions as well as the presence of additional atoms and impurities placed out of the basal plane [73,74].

3.2. Characterization of CCTO-rGO composites

3.2.1. (Micro)structural characterization

Fig. 4 (a) shows diffractograms for all CCTO-rGO composites. For all samples, the CCTO structure was indexed by a cubic perovskite phase (ICSD# 259849) with space group $Im\overline{3}$. No secondary phases peaks were identified with rGO addition. rGO peaks, generally reported at 24.76°, 42.85°, and 78.17° are not apparent in the composite diffractograms, which may be explained by their low crystallinity.
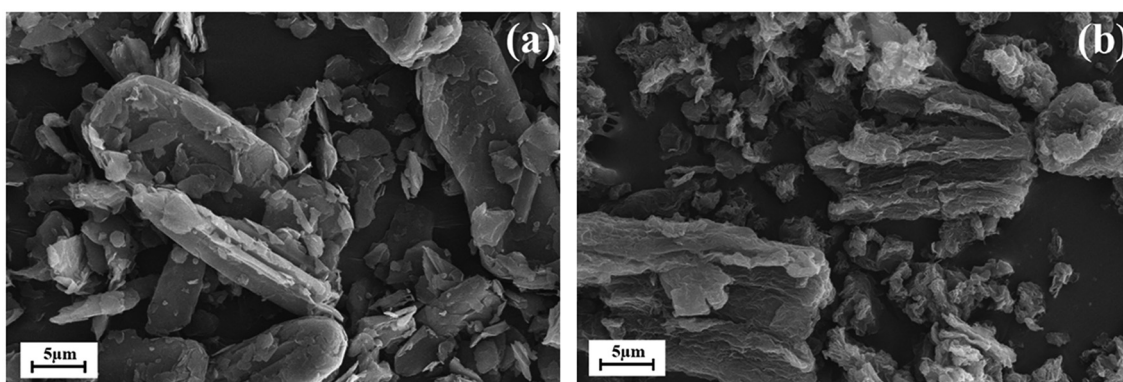

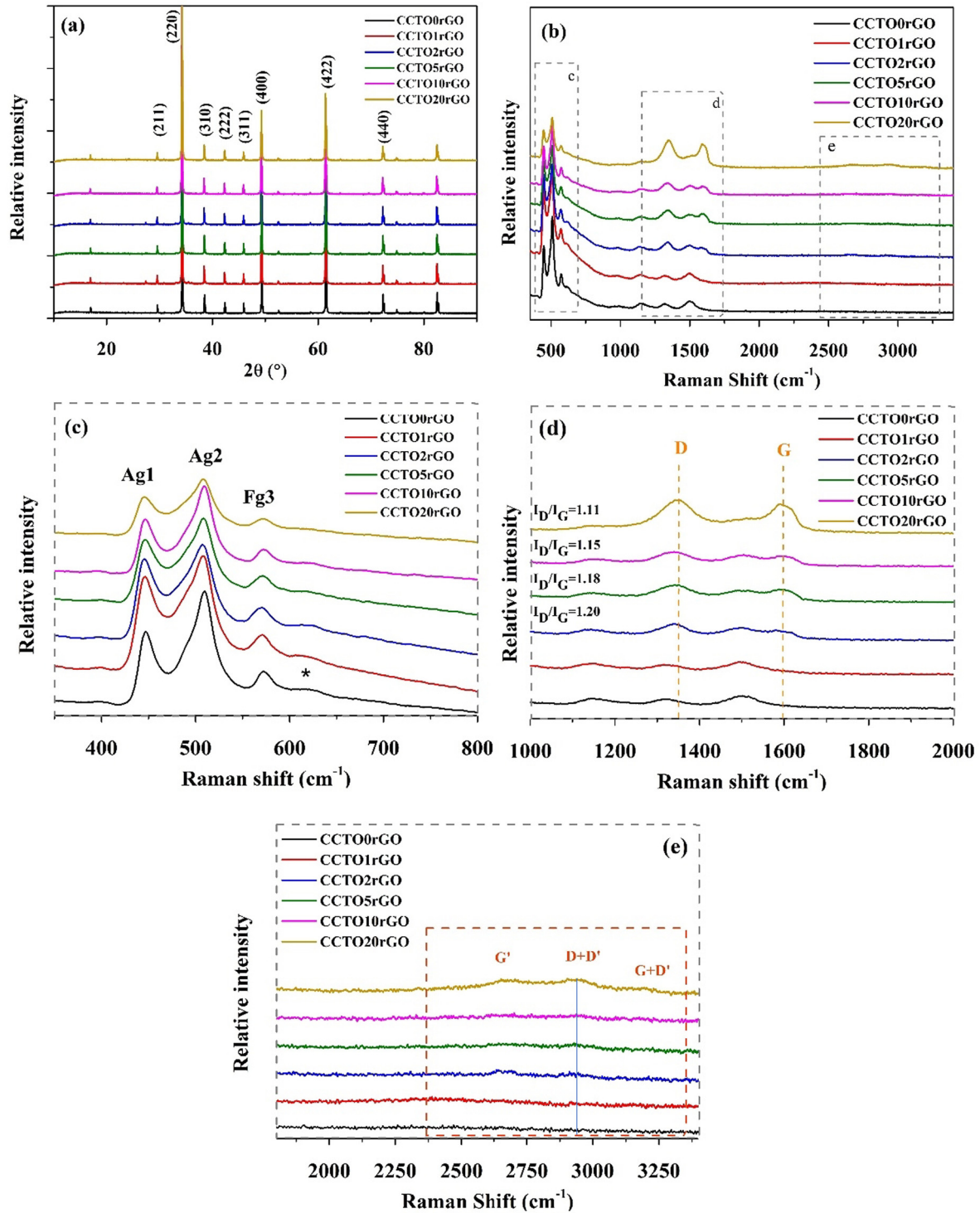**Fig. 3.** SEM micrographs of (a) graphite and (b) rGO.

Fig. 4. (a) Diffractograms of CCTO-rGO composites, (b) Raman spectra of CCTO-rGO composites with highlighted modes of (c) CCTO, and (d), (e) rGO. The * represents the TiO_2 mode.

Lattice parameters associated with the CCTO phase showed no significant changes according to *Rietveld* analysis. Table S1 summarizes all geometric and *Rietveld* parameters for the CCTO phase, indicating a coherent, reliable structural refinement in accordance with the literature [75].

Fig. 4(b) exhibits Raman spectra for all the CCTO-rGO composites. Fig. 4(c) shows the spectra region between 350 and 800 cm^{-1} and reveals four out of the eight common Raman-active vibrational modes associated with the CCTO structure ($2A_g + 2E_g + 4F_g$). The first

vibrational modes identified experimentally were located at 445 cm^{-1} (A_{1g}), ~ 510 cm^{-1} (A_{2g}) and ~ 619 cm^{-1} (A_{1g}), which can be related to rotating [TiO_6] octahedra within the CCTO structure [76,77]. Analogously, the mode at 574 cm^{-1} (F_{3g}) corresponds O–Ti–O anti-stretching vibrations of [TiO_6] clusters [31]. These results are in accordance with the literature [78,79]. Finally, modes located at ≈1150 and ≈ 1310 cm^{-1} may be associated with phononic vibrations in the CCTO structure [79]. Fig. 4(d) exhibits bands D and G associated with the rGO structure (≈ 1350 and ≈ 1586 cm^{-1}, respectively) (see

Table 1
Raman modes of the CCTO-rGO composites.

	Mode	Motion description	Observed wave number (cm^{-1})
CaCu$_3$Ti$_4$O$_{12}$	A$_{1g}$	TiO$_6$ rotation	~445
	A$_{2g}$	TiO$_6$ rotation	~510
	F$_{3g}$	O - Ti - O antisymmetric stretching	~574
rGO	D (A$_{1g}$)	Vibration of disordered C$_{(graphite)}$ atoms with dangling bonds in plane terminations, which corresponds to the breathing mode	~1350
	G (E$_{2g}$ mode)	Vibration of sp^2-bonded carbon atoms at Γ-point in two-dimensional hexagonal lattices	~1586
	G*		~2625
	D + D′	Only clear for CCTO20rGO	~2937
	G + D′		~3250
TiO$_2$	A$_g$(1)	O - Ti – O stretching	~619

F.M. Praxedes[1]*, H. Moreno[1], A.Z. Simões[1], V.C. Teixeira[2], R.S. Nunes[1], R.A.C. Amoresi[1], M.A. Ramirez[1].

Fig. 1c), which become apparent for an rGO content greater than 2%. Band D can be associated with sp^2-bonded carbon atoms vibrations in the two-dimensional hexagonal lattice, while band D indicates disorder-induced by structural defects and is related to vibration of C$_{(graphite)}$ atoms with dangling bonds in the plane terminations [80]. The calculated I$_D$/I$_G$ ratio indicates an increase in defect density with increasing rGO content, which may be a result of the physical interaction between rGO particles within the CCTO ceramic matrix [61]. Finally, bands G*, D + D′, and G + D′ do not appear clearly in the Raman spectra of the composites. Fig. 4(e) shows these bands are only clear for CCTO20rGO, corroborating XRPD data, which show lower intensity for the rGO peaks diffracted in the composites. Table 1 summarizes the vibrational modes characterizing the structure of CCTO-rGO composite systems.
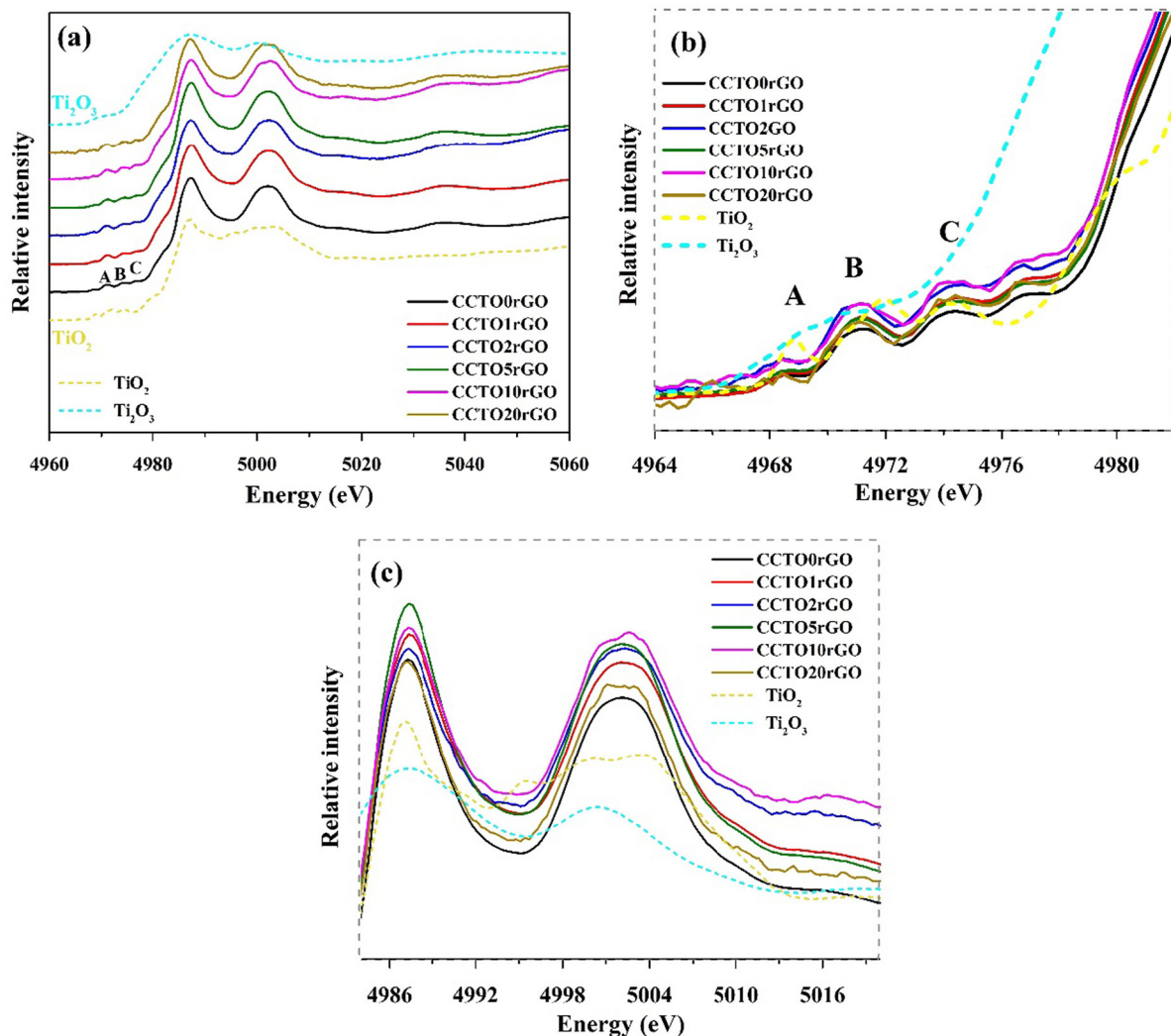
Fig. 5. (a) XANES spectrum of CCTO-rGO with a zoom of the (b) pre-edge and (c) edge region.

Fig. 5(a-c) displays XANES spectra measured at the Ti K-edge for all CCTO-rGO composites. Fig. 5(a) shows the occurrence of pre-edge peaks (A, B, C) directly related to octahedrally coordinated Ti^{4+} to form $[TiO_6]$ in the CCTO structure. Fig. 5(b) highlights the pre-edge (A, B, C) structures. According to Oliveira et al. [81], peak A (~ 4968 eV) is caused by quadrupolar excitation of electrons between the orbitals $1s$ and t_{2g} in the absorbent octahedral cluster $[TiO_6]$, while peak B (~4971 eV) is due to the electronic transitions from $1s$ to the p-d hybrid states. Finally, peak C (~ 4974 eV) is related to the dipolar excitations of Ti $1s$ electrons and t_{2g} states in neighboring $[TiO_6]$ octahedra. An increase in the intensity associated with peak C indicates that changes in the $[TiO_6]$ clusters towards a non-centered octahedron. Thus, the addition of rGO to CCTO in the composites did not affect the centrosymmetry of the $[TiO_6]$ clusters. The area under the B peaks is proportional to the concentration of clusters, which indicates octahedral distortion and is critical for the photocatalytic response. The insert in Fig. 5(c) exhibits the first oscillations after the edge region (~ 4985 to 5010 eV). In the spectra of CCTO-rGO samples, no shifts or emergence of new peaks can be observed in the composites compared to CCTO0rGO. However, changes in first oscillation intensities and peak

areas were noted; in turn, linear combination fitting was considered for oxidation state analysis. Through fittings of the curves, one may note that there is a greater correspondence between the composites and TiO_2 curve, suggesting the dominance of the Ti^{4+} oxidation state in the samples [82].

Fig. 6(a-f) reveals SEM micrographs for all CCTO-rGO composites. The white circles highlight rGO particles with lamellar morphology spread within the CCTO matrix. The rGO phase appears well dispersed within the CCTO particles, hence, SEM shows no clear signs of effective CCTO-rGO interaction. This observation corroborates the results obtained in the structural analyses, in which bonds between the CCTO and C were not identified. This may be the result of particle size, which is on the micrometric scale; as highlighted by Mohammed et al. [83], powders in nanometric granulometry are more easily adsorbed on the surface of other particles.

Fig. 7(a-f) shows adsorption–desorption isotherms as well as surface area, pore size, and pore volume values for the $CaCu_3Ti_4O_{12}$/rGO composites system. All samples reveal type III isotherms, characteristic of non-porous particles, in which there is high adsorbate-solid interaction [84–86]. The results indicate the formation of mesoporous particles
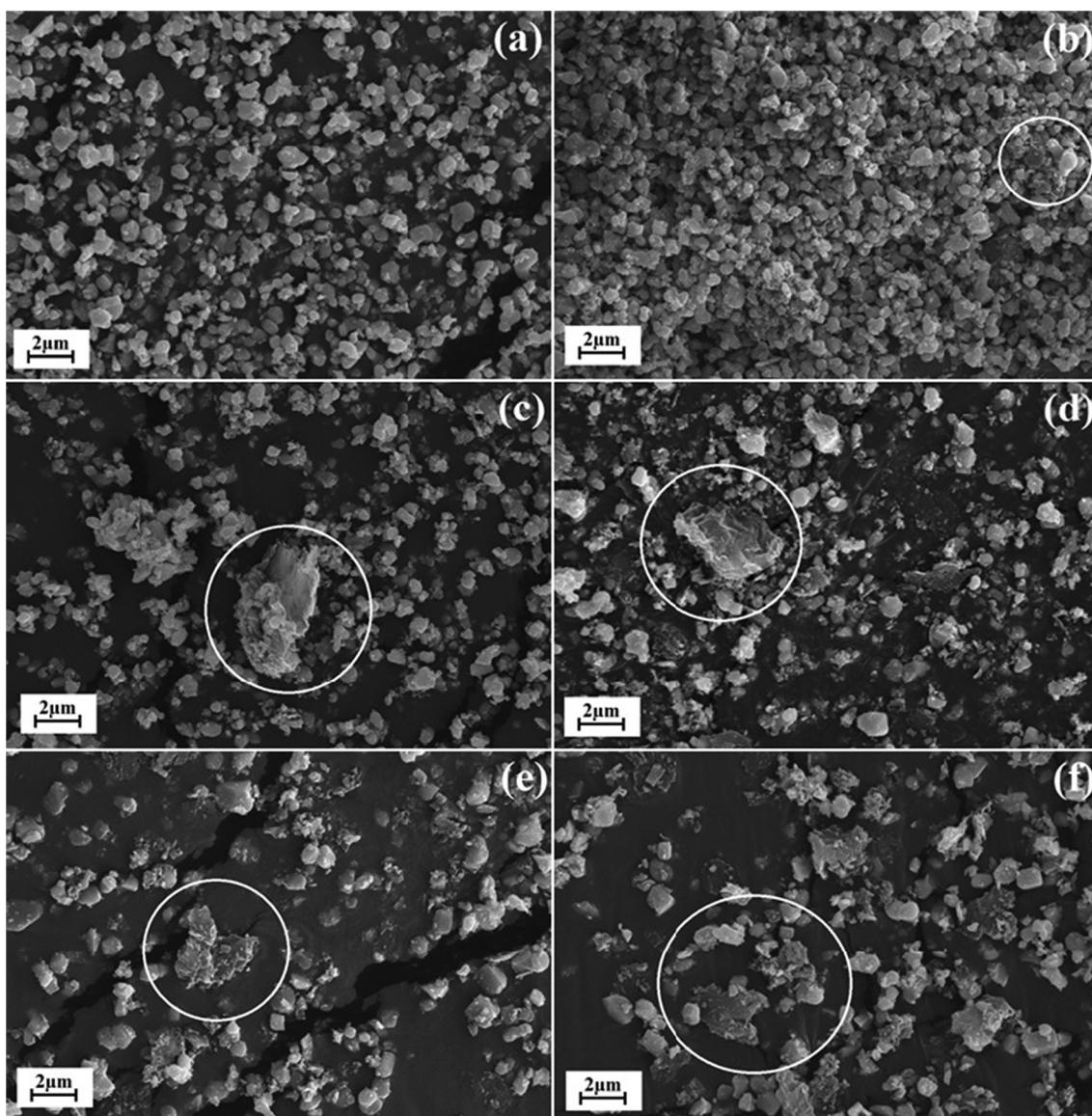

Fig. 6. Scanning electron microscopy of the samples (a) CCTO0rGO (b) CCTO1rGO, (c) CCTO2rGO, (d) CCTO5rGO, (e) CCTO10rGO and (f) CCTO20rGO. rGO highlighted by white circles.
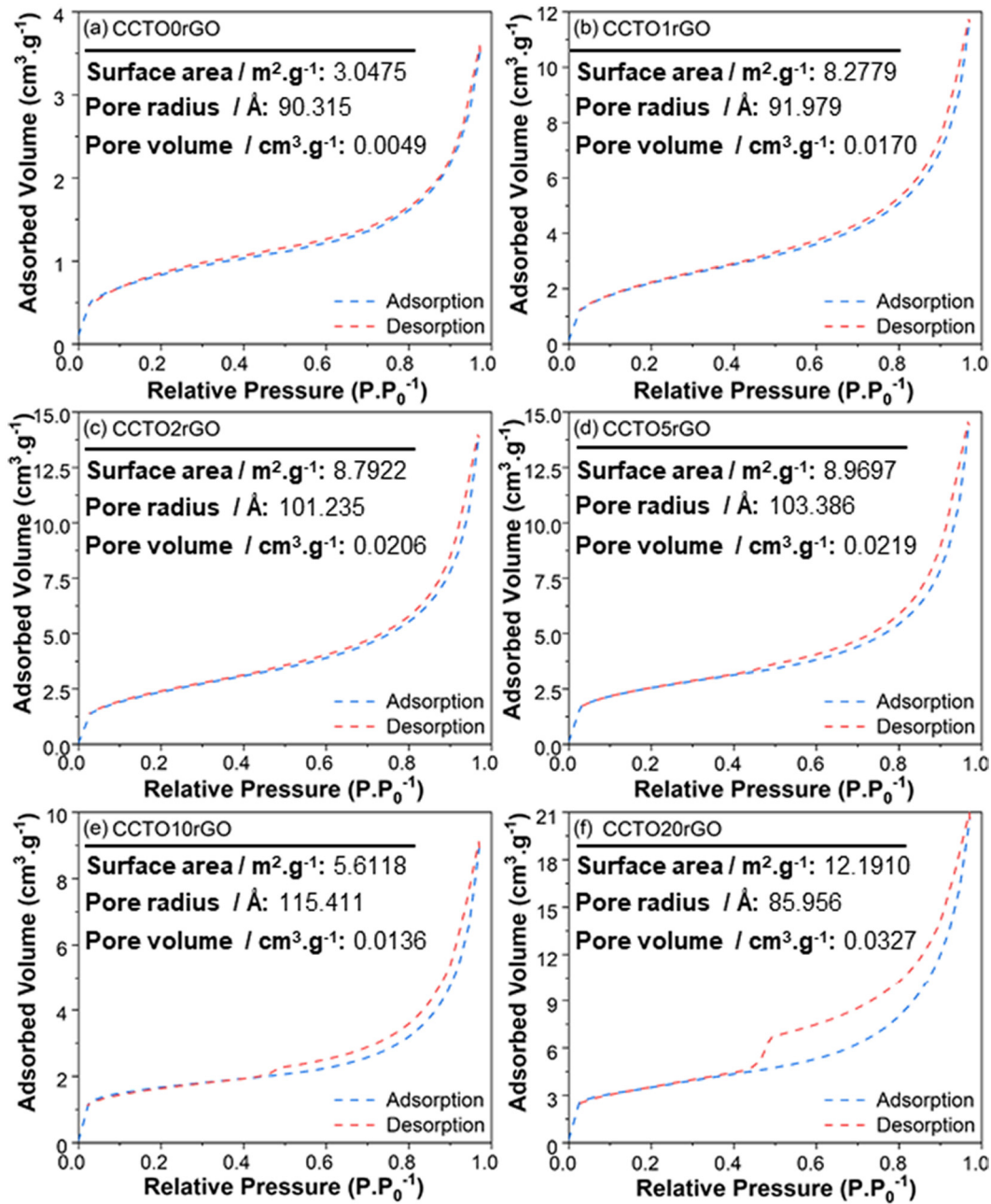
Fig. 7. Textural properties obtained for samples (a) CCTO0rGO (b) CCTO1rGO, (c) CCTO2rGO, (d) CCTO5rGO, (e) CCTO10rGO and (f) CCTO20rGO using the B.E.T. method.

$(20 < \phi < 500 \text{ Å})$ [85]. The combination of low pore volume and type III isotherms may be associated with the presence of lamelar-like rGO particles spread within the CCTO matrix, leading to the formation of slit-shaped pores. The B.E.T. results show a significant surface area increase, which may be evidence of more active sites for anchorage of the anionic dye and, in turn, leading to a higher adsorption capacity of sample CCTO20rGO compared to CCTO0rGO.

3.2.2. Optical characterization

Fig. 8(a) shows reflectance vs. wavelength plots for all CCTO-rGO composites. All results indicate maximum reflectance range centered at 600 nm and increasing rGO content in the composites significantly decreases reflectance. This may be attributed to darkened color of rGO powder (black) added to CCTO (orange), favoring self-absorption. In Fig. 8(b), $(\alpha h\nu)^2$ vs. E plots all samples that correspond to a bandgap close to ~2.3 eV (Fig. S3). This study's results reveal slight changes in

the bandgap energy as a result of rGO addition. For sample CCTO20rGO, a 0.6 eV bandgap energy decrease suggests higher order/disorder effect possibly related to CCTO-rGO interactions [83,87]. These findings are in accordance with the literature, which reports a red-shift caused by rGO/CNTs addition to TiO_2, indicating bandgap narrowing and Ti-O-C bond formation [41].

Fig. 8(c) displays PL emission spectra for all CCTO-rGO composites. Initially, PL emission intensity increases for rGO contents up to 5%. For rGO contents ≥10% PL quenching is observed, which may be a result of higher self-absorption due to rGO addition, which is in agreement with reflectance spectroscopy results (Fig. 8a). Additionally, carbonaceous compounds tend to increase conductivity through sp^2 domain reconstitution, decreasing electron retention capacity and, thus, PL intensity, as reported by Krishnamoorthy et al. [88]. The observed PL intensity drop for samples CCTO10rGO and CCTO20rGO may also derive from donor-acceptor electronic transitions and/or the presence of
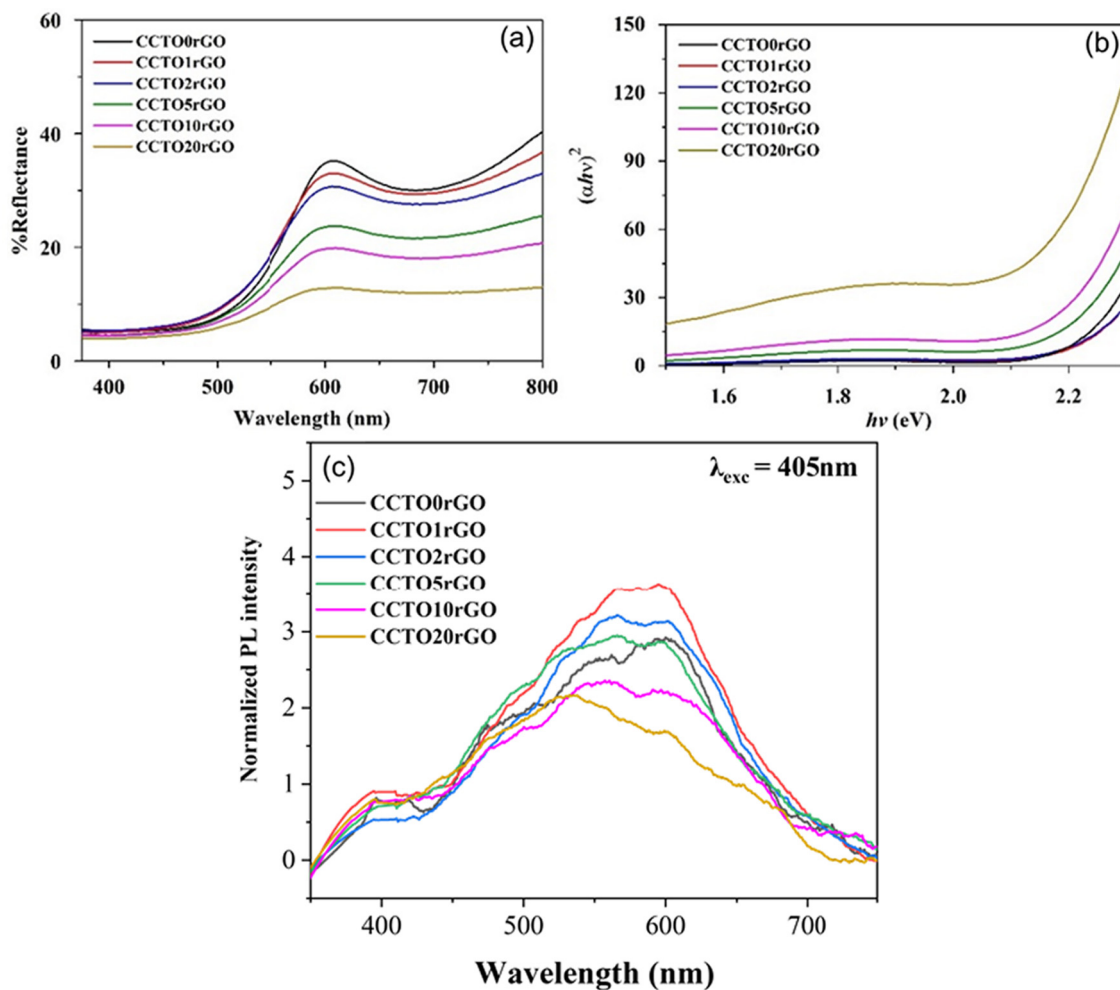
Fig. 8. (a) Reflectance curves and (b) Tauc plots for all CCTO/rGO composites, and (c) PL spectra for all CCTO-rGO composites.

defect states, leading to nonradiative recombination [89,90], which is already probable for CCTO-rGO composite systems due to charge separation on new surface states. Sun et al. [25] associated quenching on TiO_2-rGO hybrid aerogels with TiO_2–rGO charge transfer, decreasing electron-hole recombination energy and improving PC efficiency [91,92].

Fig. 9(a-f) exhibits deconvoluted PL spectra for all CCTO-rGO composites and its respective emission color percentage breakdown is presented in Table 2. One can observe an increase in the violet region emissions and a decrease in the orange-red region. This shift towards violet emissions suggests that rGO reduces the presence of deep defects in these composites. Violet region emissions in CCTO may be favored by rGO intrinsic emissions since it increases with rGO content, especially for higher concentrations (10% and 20% rGO), as well as by higher availability of free excitons in the CCTO structure due to rGO capacity to act as an electron donor [88]. The suppression of orange-red emissions of CCTO [88] may be associated with the relaxation of conduction band (CB) electrons and the transference of holes from the valence band (VB) to the carbon material [88,93,94].

Fig. 10 illustrates rGO dual behavior, which acts as an electron donor/acceptor. The literature shows that rGO can trap charges from particles by the transportation of CB electrons and VB holes [49]. Additionally, deep-level defects like Ti^{3+} and oxygen vacancies, which could promote orange-red emissions, improve charge mobility, and deteriorate the recombination process [88]. However, these defects can be distributed in the particle surface and its defects can react with rGO

functional groups promoting its passivation [94]. This phenomenon can explain the orange-red emission reduction once these deep defects are neutralized.

Fig. 11(a-d) displays adsorption and photocatalytic tests under UV radiation. Fig. 11(a) shows the adsorbed/photodiscolored RhB concentration as a function of time. The regions labeled as dark and "light" in Fig. 11(a) and Fig. 11(c) indicate adsorption and photodiscoloration behaviors, respectively. It is observed from Fig. 11(a) that, from the addition of 2% of rGO, there is an increase in the adsorption capacity of the material, reaching ~26% of adsorption for the CCTO20rGO material. This fact can be associated with larger particle surface area and pore volume according rGO concentration increase, verified in the B.E.T. results (Fig. 7). These results confirm the formation of a composite and expand the applicability range of our material for future performance as an adsorbent material [95]. Sample CCTO20rGO showed the highest adsorption capacity, proportion of adsorption, and discoloration percentage compared to all other composites. Fig. 11(b) shows ln A/A_0 vs. reaction time plots, from which one can obtain reaction constant (k) values, shown in Table 3. The adsorption, photodiscoloration and half-life values, $t_{1/2}$, calculated from the samples are also shown in Table 3. To demonstrate the half-life time, a longer photocatalytic test was performed for the CCTO20rGO sample (Fig. S5), experimentally proving the calculated result.

Some authors have shown that increasing rGO content could reduce photocatalytic activity due to the lower number of electron pairs and holes [42], creating some sort of shielding effect and limiting UV–vis
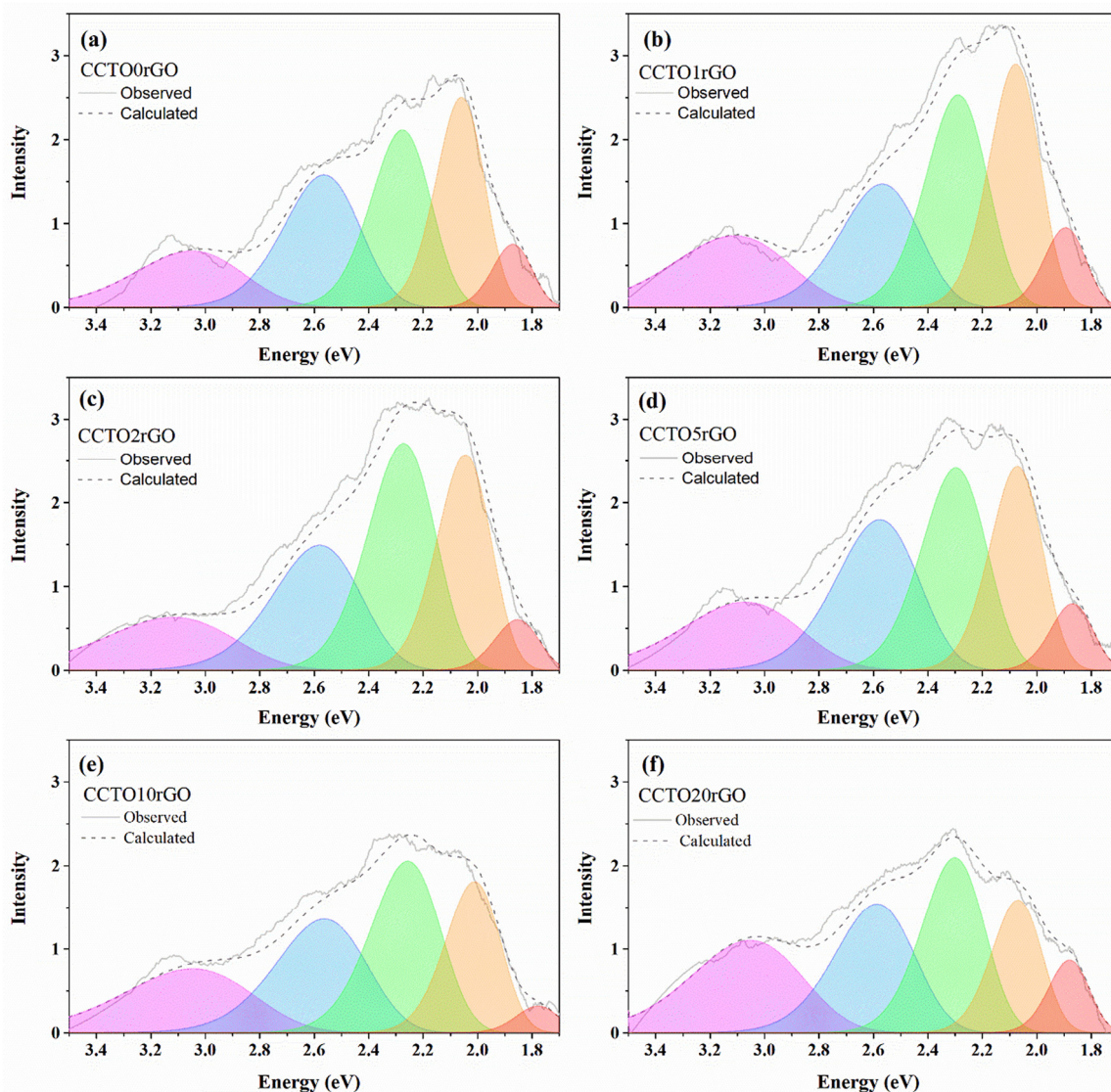
Fig. 9. Photoluminescence spectra and deconvolution of samples (a) CCTO0rGO, (b) CCTO1rGO, (c) CCTO2rGO, (d) CCTO5rGO, (e) CCTO10rGOe (f) CCTO20rGO.

light absorption by nanoparticles [43,95]. Shah et al. [96] demonstrated the importance of high surface area/active surface sites in the catalytic activity of rGO compounds. On the other hand, surface area increase due to rGO addition can enhance adsorption. Yan et al. [97] found out that GO can adsorb cationic molecules such as RhB due to GO-dye strong (π-π) interactions. Hence, to maximize photocatalytic activity CCTO-rGO composites one needs to closely control particle growth kinetics (morphology, surface-to-volume ratio, etc.) and matrix-to-load ratio composite ratio. CCTO20rGO exhibits rapid RhB removal in the first

minutes of reaction without irradiation, corroborating the hypothesis of dye adsorption by the composite, according to the data in Table 3.

Fig. 11(c) displays adsorption-photodiscoloration stability curves for the CCTO20rGO sample. CCTO20rGO adsorption capacity (dark labeled region) showed no signs of deterioration after each cycle. Regarding photodiscoloration (light labeled region), following the second cycle there is a slight increase in CCTO20rGO photodiscoloration capacity (last cycle 5% higher compared to the initial cycle), manifesting no photodiscoloration deactivation but a slight increase. Additionally, XRPD analysis performed after the cycles (Fig. 11d) indicate that although the CCTO phase remains present, its peak intensity compared to sample CCTO20rGO before PC cycles decreases significantly. Additionally, the insert in Fig. 11(d) shows strong peak displacement towards lower 2θ values, indicating lattice expansion in the composite after submitted to PC cycles.

These results may indicate that PC cycles promote rGO-CCTO interaction altering the CCTO particles exposed surface [98,99] between the *hk*0 and *h*00 planes (Fig. 11e,) with more [CuO$_4$] clusters present in the surface. Hence, the authors expect an increase in rGO-CCTO interaction due to improved charge transfer process, which reflects in the best photodiscoloration capacity. However, further analysis should be performed in the future to prove this statement.

Table 2
Color contribution percentages of in the photoluminescence spectra.

Sample	Violet (%)	Blue (%)	Green (%)	Orange (%)	Red (%)
CCTO0rGO	8.7	20.8	27.8	32.9	9.9
CCTO1rGO	9.5	17.0	29.2	33.4	10.9
CCTO2rGO	7.5	18.7	34.0	32.3	7.5
CCTO5rGO	9.6	21.8	29.4	29.6	9.6
CCTO10rGO	11.8	21.7	32.5	28.9	4.7
CCTO20rGO	14.9	21.6	29.3	22.2	12.1

F.M. Praxedes[1*], H. Moreno[1], A.Z. Simões[1], V.C. Teixeira[2], R.S. Nunes[1], R.A.C. Amoresi[1], M.A. Ramirez[1].
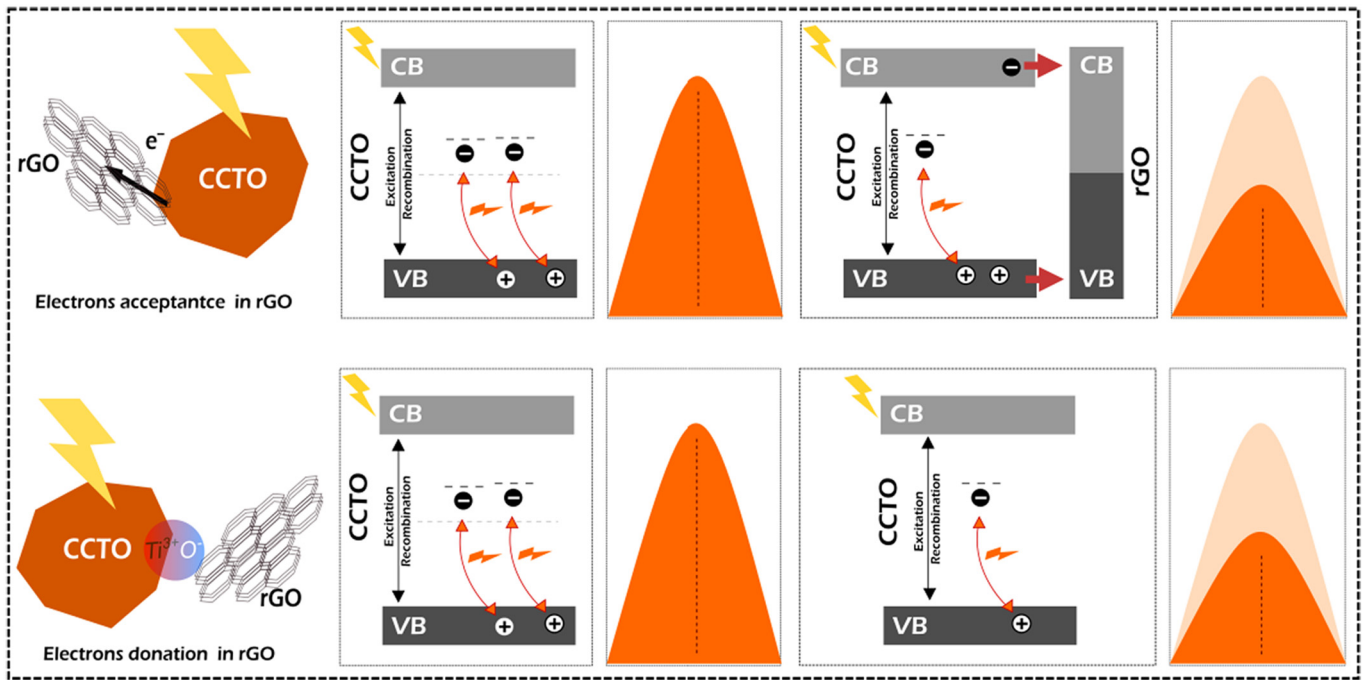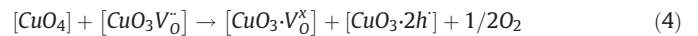
Fig. 10. Mechanism of reduction in the emission of orange region.

Fig. 11(e) exhibits trapping experiment results for CCTO0rGO and the most efficient composite (CCTO20rGO). To verify which agent produces photocatalytic activity in CCTO-rGO composites, isopropanol (IPA), disodium EDTA (EDTA), and p-benzoquinone (BQ) were added to function as OH^{-*}, h$^+$, and O$_2^*$ species trapping agents, respectively [62]. For sample CCTO0rGO, the addition of isopropanol during photocatalysis generates hydroxyl radicals (OH^{-*}) as scavengers and causes slight photocatalytic change (~ 3%). On the other hand, EDTA/ BQ leads promotes holes (h$^+$) and superoxide radicals (O$_2^*$) scavengers, respectively, significantly increasing photocatalytic activity when sequestered, mainly with O$_2^*$ (~ 82%) species. The same behavior can be observed for low bandgap energy/high charge carrier (e$^-$/h$^+$) recombination rate materials [26,99]. When EDTA (h$^+$ scavengers) is added, photocatalytic activity decreases from 27% to 20%. This suggests that, in the composite materials, h$^+$ species are subject not only to electron-hole recombination, as seen with CCTO0rGO, but it also has an effective participation in the photocatalytic process, probably due to rGO interaction and the active sites on the CCTO surface. Furthermore, holes (h$^+$) are in resonance with carbon sp^2 bonds of rGO as demonstrated by PL results (Fig. 9), which interferes with photocatalytic efficiency.

Our results, both from the active species trapping experiments and crystalline planes exposed after the photocatalytic cycles, showing the influence of copper clusters to improve photocatalytic activity, can be associated with the engineering of charge carrier transfer process in CCTO-rGO composites. CCTO-rGO interaction, as observed in PC and PL analyses, leads to the formation of radicals (e.g., $^*O_2^-$) (Eq. (3)), and intensifies [CuO$_4$] cluster influence towards these properties [100], generating holes (Eq. (4)) [101] in the composite material and, thus, increasing its photocatalytic activity.

$$rGO\ (e^-) + O_2 \rightarrow rGO + {}^{\bullet}O_2^- \tag{3}$$

$$[CuO_4] + [CuO_3V_O^{\cdot\cdot}] \rightarrow [CuO_3 \cdot V_O^x] + [CuO_3 \cdot 2h^{\cdot}] + 1/2O_2 \tag{4}$$

Future analyses with the targeted growth of CCTO-rGO composites should be carried out in order to better analyze this interaction. Additionally, with the aim of deepening understanding on the material photocatalytic behavior, degradation tests with a colorless pollutant, cyproflaxin (CIP), were performed (Fig. S6). An antibiotic frequently detected in wastewater [102], CIP shows absorption bands in the regions of 275 nm and 315–330 nm corresponding to π → π* and non-binding → π* transitions. The degradation curves show that the materials affected the CIP molecules composed mainly of n → π* absorption bands. Kushwaha et al. [103] has shown promising photocatalytic results using CCTO pellets under visible light for the degradation of colorless pollutants. For future purposes, efforts should be focused on verifying the influence of controlled targeting of nanoparticles and CCTO-rGO nanocomposites, activity in visible light/UV, and charge transfer mechanisms on photocatalytic activity.

4. Conclusions

Structural investigations reveal that through the methodology used in this study, the structure and morphology of the CCTO are preserved without significant changes due to the presence of rGO. However, changes in the PL response due to an increase in rGO content suggest that rGO can present secondary bonds with CCTO, acting as a donor/acceptor of electrons. Sample CCTO20rGO showed the highest adsorption capacity compared to all other samples. The other composite samples show a PC behavior comparable to that of CCTO0rGO. This may demonstrate that, in order to promote a synergistic interaction between CCTO and rGO in the composite, there is a minimum/specific CCTO-rGO ratio which needs to be respected. The photocatalytic activity of CCTO20rGO is more efficient compared to all other composites (photodiscoloration
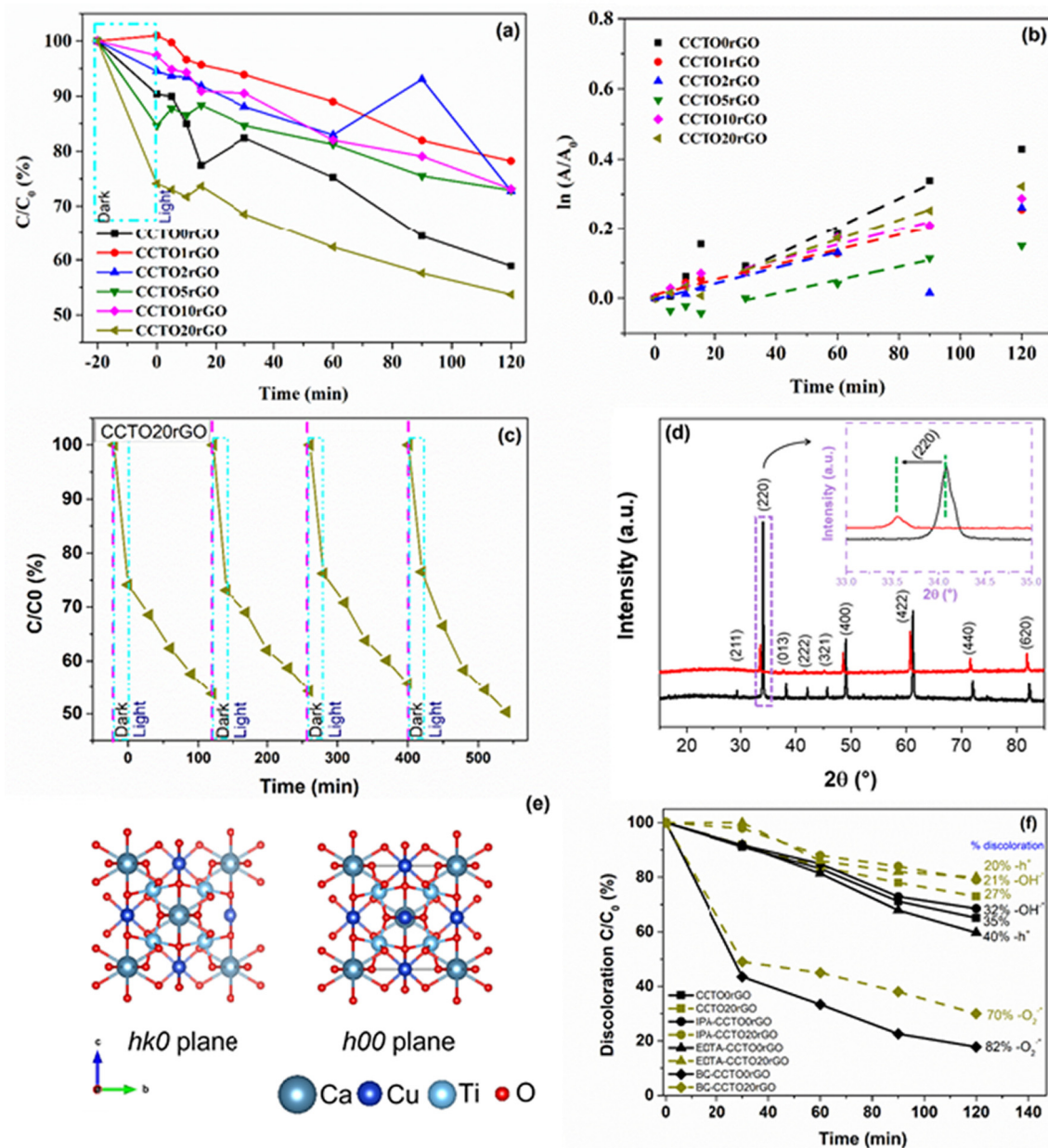
Fig. 11. (a) Degradation curve and (b) dye degradation constant (k) for all CCTO-rGO composites. (c) CCTO20rGO recycling performance and (d) Diffractograms of CCTO-rGO composites after the photocatalytic cycles (e) Main diffraction planes in the CCTO-rGO composites (f) CCTO0rGO (solid lines)/CCTO20rGO (dashed lines) trapping tests for different scavenger species during RhB photodegradation.

Table 3
Adsorption, photodiscoloration and total removal percentages for CCTO-rGO composites in photocatalytic tests with its related constant of photodiscoloration (k) and half-life ($t_{1/2}$).

Samples	Adsorption (%)	Discoloration$_{120}$ (%)	Total (%)	k x 10^{-3} (min^{-1})	$t_{1/2}$ (min)
CCTO0rGO	9.64	34.84	41.12	4.11	168.65
CCTO1rGO	0.00	21.79	21.79	2.15	322.39
CCTO2rGO	5.50	23.00	27.24	2.25	322.39
CCTO5rGO	15.37	13.86	27.10	1.91	362.90
CCTO10rGO	2.63	24.87	26.85	2.25	308.06
CCTO20rGO	25.88	27.57	46.31	2.90	239.01

F.M. Praxedes[1*], H. Moreno[1], A.Z. Simões[1], V.C. Teixeira[2], R.S. Nunes[1], R.A.C. Amoresi[1], M.A. Ramirez[1].

constant of 2.90×10^{-3}). Considering total removal (adsorption and photodiscoloration effects), the CCTO20rGO composite is the most efficient discoloring agent. This study's results show CCTO-rGO composites may be a promising choice for future UV–visible light-driven photocatalytic devices with high adsorption/lower response time. Additionally, the possibility to trigger photocatalysis by sunlight makes it an important step towards achieving sustainability in water purification methods.

CRediT authorship contribution statement

F.M. Praxedes: Conceptualization, Methodology. **H. Moreno:** Formal analysis. **A.Z. Simões:** Formal analysis, Writing – review & editing. **V.C. Teixeira:** Formal analysis, Writing – review & editing. **R.S. Nunes:**

Writing – review & editing. **R.A.C. Amoresi:** Formal analysis, Writing – review & editing. **M.A. Ramirez:** Conceptualization, Methodology, Supervision.

Declaration of Competing Interest

The authors declare that they have no known competing financial interests or personal relationships that could have appeared to influence the work reported in this paper.

Appendix A. Supplementary data

Supplementary data to this article can be found online at https://doi.org/10.1016/j.powtec.2022.117478.

References

[1] M.A. Subramanian, et al., High dielectric constant in $ACu_3Ti_4O_{12}$ and $ACu_3Ti_3FeO_{12}$ phases, J. Solid State Chem. 151 (2000) 323–325.

[2] K. Prompa, et al., Very high performance dielectric and non-Ohmics properties of $CaCu_3Ti_{4.2}O_{12}$ ceramics for X8R capacitors, Ceram. Int. 44 (2018) 13267–13277.

[3] E.C. Grzebielucka, et al., Improvement in varistor properties of $CaCu_3Ti_4O_{12}$ ceramics by chromium addition, J. Mater. Sci. Technol. 41 (2020) 12–20.

[4] J. Jumpatam, et al., Improved giant dielectric properties of $CaCu_3Ti_4O_{12}$ via simultaneously tuning the electrical properties of grains and grain boundaries by F- substitution, RSC Adv. 7 (2017) 4092–4101.

[5] H. Lin, et al., Origin of high dielectric performance in fine grain-sized $CaCu_3Ti_4O_{12}$ materials, J. Eur. Ceram. Soc. 40 (2020) 1957–1966.

[6] Z. Peng, et al., A new perovskite-related ceramic with colossal permittivity and low dielectric loss, J. Eur. Ceram. Soc. 40 (2020) 4010–4015.

[7] P. Thongbai, et al., Improved dielectric and non-ohmic properties of $Ca_2Cu_2Ti_4O_{12}$ ceramics prepared by a polymer pyrolysis method, J. Alloys Compd. 509 (2011) 7416–7420.

[8] N. Zhao, et al., Temperature stability and low dielectric loss of lithium-doped $CdCu_3Ti_4O_{12}$ ceramics for X9R capacitor applications, Ceram. Int. 45 (2019) 22991–22997.

[9] S. Bellani, et al., Carbon-based photocathode materials for solar hydrogen production, Adv. Mater. 31 (2019) (Article 1801446).

[10] X. Zhang, et al., Thin film perovskite light-emitting diode based on $CsPbBr_3$ powders and interfacial engineering, Nano Energy 37 (2017) 40–45.

[11] M. Patel, et al., Transparent all-oxide photovoltaics and broadband high-speed energy-efficient optoelectronics, Sol. Energy Mater. Sol. Cells 194 (2019) 148–158.

[12] N. Tsvetkov, et al., Synthesis of Nanocrystalline $Nb:SrTiO_3$ Electron transport layers for robust interfaces and stable high photovoltaic energy conversion efficiency in perovskite halide solar cells, ACS Appl. Energy Mater. (2019) 344–351.

[13] J. Chen, et al., Functional rGO aerogel as a potential adsorbent for removing hazardous hexavalent chromium: adsorption performance and mechanism, Environ. Sci. Pollut. Res. 27 (2020) 10715–10728.

[14] V. Kumar, et al., Potential applications of graphene-based nanomaterials as adsorbent for removal of volatile organic compounds, Environ. Int. 135 (2020) (Article 105356).

[15] G.U. Rehman, et al., Controlled synthesis of reduced graphene oxide supported magnetically separable $Fe_3O_4@rGO@AgI$ ternary nanocomposite for enhanced photocatalytic degradation of phenol, Powder Technol. 356 (2019) 547–558.

[16] Q. Nie, et al., High piezo–catalytic activity of $ZnO/Al2O3$ nanosheets utilizing ultrasonic energy for wastewater treatment, J. Clean. Prod. 242 (2020) (Article 118532).

[17] S. Yang, et al., Flexible and reusable non-woven fabric photodetector based on Polypyrrole/crystal violet lactone for NIR light detection and writing, Adv. Fiber Mater. 2 (2020) 150–160.

[18] C. Wang, et al., Facile construction of novel organic–inorganic tetra (4-carboxyphenyl) porphyrin/Bi_2MoO_6 heterojunction for tetracycline degradation: performance, degradation pathways, intermediate toxicity analysis and mechanism insight, J. Colloid Interface Sci. 605 (2022) 727–740.

[19] S. Li, et al., Synthesis of Ta_3N_5/Bi_2MoO_6 core-shell fiber-shaped heterojunctions as efficient and easily recyclable photocatalysts, Environ. Sci.: Nano. 4 (2017) 1155–1167.

[20] J. Li, et al., Clues to the giant dielectric constant of $CaCu_3Ti_4O_{12}$ in the defect structure of "$SrCu_3Ti_4O_{12}$", Chem. Mater. 16 (2004) 5223–5225.

[21] Q. Guo, et al., Fundamentals of TiO2 Photocatalysis: concepts, mechanisms, and challenges, Adv. Mater. 31 (2019) 1–26.

[22] J.H. Clark, et al., Visible light photo-oxidation of model pollutants using $CaCu_3Ti_4O_{12}$: an experimental and theoretical study of optical properties, electronic structure, and selectivity, J. Am. Chem. Soc. 133 (2011) 1016–1032.

[23] S. Xiong, et al., Growth of $AgBr/Ag_3PO_4$ heterojunction on chitosan fibers for degrading organic pollutants, Adv. Fiber Mater. 2 (2020) 246–255.

[24] G. Duoerkun, et al., Construction of $n-TiO_2/p-Ag_2O$ junction on carbon Fiber cloth with Vis–NIR Photoresponse as a filter-membrane-shaped Photocatalyst, Adv. Fiber Mater. 2 (2020) 13–23.

[25] Y. Sun, et al., Enhanced photocatalytic performance of surface-modified TiO2 nanofibers with Rhodizonic acid, Adv. Fiber Mater. 2 (2020) 118–122.

[26] R.A.C. Amoresi, et al., CeO_2 nanoparticle morphologies and their corresponding crystalline Planes for the photocatalytic degradation of organic pollutants, ACS Appl. Nano Mater. 2 (2019) 6513–6526.

[27] J. Luo, et al., A critical review on energy conversion and environmental remediation of Photocatalysts with remodeling crystal lattice, surface, and Interface, ACS Nano 13 (2019) 9811–9840.

[28] A.A. Felix, et al., Probing the effects of oxygen-related defects on the optical and luminescence properties in $CaCu_3Ti_4O_{12}$ ceramics, J. Eur. Ceram. Soc. 38 (2018) 5002–5006.

[29] J. Jumpatam, et al., Influences of $Sr2+$ doping on microstructure, giant dielectric behavior, and non-Ohmic properties of $CaCu_3Ti_4O_{12}/CaTiO_3$ ceramic composites, Molecules. 26 (2021) 1–13.

[30] J. Jumpatam, et al., Significantly improving the giant dielectric properties of $CaCu_3Ti_4O_{12}$ ceramics by co-doping with Sr^{2+} and F^- ions, Mater. Res. Bull. 133 (2021) (Article 111043).

[31] H. Moreno, et al., Tunable photoluminescence of $CaCu3Ti4O12$ based ceramics modified with tungsten, J. Alloys Compd. 850 (2021) (Article 156652).

[32] R. Hailili, et al., Oxygen vacancies induced visible-light photocatalytic activities of $CaCu_3Ti_4O_{12}$ with controllable morphologies for antibiotic degradation, Appl. Catal. B Environ. 221 (2018) 422–432.

[33] R. Hailili, Z.Q. Wang, X.Q. Gong, C. Wang, Octahedral-shaped perovskite $CaCu3Ti4O12$ with dual defects and coexposed {(001), (111)} facets for visible-light photocatalysis, Appl. Catal. B Environ. 254 (2019) 86–97.

[34] P. Saikia, et al., Synthesis of $CaxCu3-xTi4O12$ perovskite materials and house-hold LED light mediated degradation of rhodamine blue dye, J. Inorg. Organomet. Polym. Mater. 31 (2021) 2161–2167.

[35] M. Ahmadipour, et al., Synthesis of core/shell-structured $CaCu3Ti4O12/SiO2$ composites for effective degradation of rhodamine B under ultraviolet light, J. Mater. Sci. Mater. Electron. 31 (2020) 19587–19598.

[36] S.J. Rowley-Neale, et al., An overview of recent applications of reduced graphene oxide as a basis of electroanalytical sensing platforms, Appl. Mater. Today 10 (2018) 218–226.

[37] D.G. Papageorgiou, et al., Mechanical properties of graphene and graphene-based nanocomposites, Prog. Mater. Sci. 90 (2017) 75–127.

[38] D.M.A.S. Dissanayake, et al., Optical limiting properties of (reduced) graphene oxide covalently functionalized by coordination complexes, Coord. Chem. Rev. 375 (2018) 489–513.

[39] L. de Marchi, et al., An overview of graphene materials: properties, applications and toxicity on aquatic environments, Sci. Total Environ. 631–632 (2018) 1440–1456.

[40] X. Li, et al., Graphene in Photocatalysis: a review, Small. 12 (2016) 6640–6696.

[41] W. Fan, et al., Nanocomposites of TiO2 and reduced graphene oxide as efficient photocatalysts for hydrogen evolution, J. Phys. Chem. C 115 (2011) 10694–10701.

[42] A. Trapalis, et al., TiO_2/graphene composite photocatalysts for NOx removal: a comparison of surfactant-stabilized graphene and reduced graphene oxide, Appl. Catal. B Environ. 180 (2016) 637–647.

[43] S. Lettieri, et al., Evidencing opposite charge-transfer processes at TiO2/graphene-related materials interface through combined EPR, photoluminescence and photocatalysis assessment, Catal. Today 315 (2018) 19–30.

[44] Y. Pu, et al., Enhancing effects of reduced graphene oxide on photoluminescence of CsPbBr3 perovskite quantum dots, J. Mater. Chem. C 8 (2020) 7447–7453.

[45] T.K. Le, et al., Relation of photoluminescence and sunlight photocatalytic activities of pure V2O5 nanohollows and V_2O_5/RGO nanocomposites, Mater. Sci. Semicond. Process. 100 (2019) 159–166.

[46] Z. Wang, et al., $La_2Zr_2O_7$/rGO synthesized by one-step sol-gel method for photocatalytic degradation of tetracycline under visible-light, Chem. Eng. J. 384 (2019) (Article 123380).

[47] F. Noori, A. Gholizadeh, Structural, optical, magnetic properties and visible light photocatalytic activity of $BiFeO_3$/graphene oxide nanocomposites, Mater. Res. Express. 6 (2020) (Article 1250g1).

[48] X. Yang, et al., rGO/Fe-doped g-C 3 N 4 visible-light driven photocatalyst with improved NO removal performance, J. Photochem. Photob. A: Chem. 375 (2019) 40–47.

[49] P. Sharma, et al., Of hierarchical ZnO nano flower on large functionalized rGO sheet for superior photocatalytic mineralization of antibiotic, Chem. Eng. J. 392 (2019) (Article 123746).

[50] M. Xu, et al., Reduced graphene oxide/$Bi4O5Br2$ nanocomposite with synergetic effects on improving adsorption and photocatalytic activity for the degradation of antibiotics, Chemosphere. 265 (2021) (Article 129013).

[51] S.J. Zou, et al., A hybrid sorbent of α-iron oxide/reduced graphene oxide: studies for adsorptive removal of tetracycline antibiotics, J. Alloys Compd. 863 (2021) (Article 158475).
[52] M.L. Baynosa, et al., Eco-friendly synthesis of recyclable mesoporous zinc ferrite@ reduced graphene oxide nanocomposite for efficient photocatalytic dye degradation under solar radiation, J. Colloid Interface Sci. 561 (2020) 459–469.
[53] N.M. Dat, et al., Synthesis of silver/reduced graphene oxide for antibacterial activity and catalytic reduction of organic dyes, Synth. Met. 260 (2020) (Article 116260).
[54] Z. Wu, et al., Effective removal of high-chroma rhodamine B over $Sn_{0.215}In_{0.38}S$/ reduced graphene oxide composite: synergistic factors and mechanism of adsorption enrichment and visible photocatalytic degradation, Powder Technol. 329 (2018) 217–231.
[55] Y. Zhang, et al., Facile synthesis of reduced-graphene-oxide/rare-earth-metal-oxide aerogels as a highly efficient adsorbent for rhodamine-B, Appl. Surf. Sci. 504 (2020) (Article 144377).
[56] Y. Vieira, et al., Reactive oxygen species-induced heterogeneous photocatalytic degradation of organic pollutant rhodamine B by copper and zinc aluminate spinels, J. Chem. Technol. Biotechnol. 95 (2019) 791–797.
[57] M.R.R. Kooh, et al., Separation of toxic rhodamine B from aqueous solution using an efficient low-cost material, *Azolla pinnata*, by adsorption method, Environ. Monit. Assess. 188 (2016) 1–15.
[59] B.H. Toby, R.B. von Dreele, GSAS-II: the genesis of a modern open-source all purpose crystallography software package, J. Appl. Crystallogr. 46 (2013) 544–549.
[60] H. Rietveld, A profile refinement method for nuclear and magnetic structures, J. Appl. Crystallogr. 2 (1969) 65–71.
[61] B. Ravel, M. Newville, Athena, Artemis, Hephaestus: data analysis for X-ray absorption spectroscopy using IFEFFIT, J. Synchrotron Radiat. 12 (2005) 537–541.
[62] S. Li, et al., Degradation of tetracycline antibiotic by a novel Bi2Sn2O7/Bi2MoO6 S-scheme heterojunction: performance, mechanism insight and toxicity assessment, Chem. Eng. J. 429 (2022) (Article 132519).
[63] D. He, et al., In-situ growth of lepidocrocite on Bi2O3 rod: a perfect cycle coupling photocatalysis and heterogeneous Fenton-like process by potential-level matching with advanced oxidation, Chemosphere. 210 (2018) 334–340.
[64] S. Min, G. Lu, Dye-sensitized reduced graphene oxide photocatalysts for highly efficient visible-light-driven water reduction, J. Phys. Chem. C 115 (2011) 13938–13945.
[65] K. Zhang, et al., Enhancing thermoelectric properties of organic composites through hierarchical nanostructures, Sci. Rep. 3 (2013) 1–7.
[66] B. Gupta, et al., Role of oxygen functional groups in reduced graphene oxide for lubrication, Sci. Rep. 7 (2017) (Article 45030).
[67] M. Li, et al., The doping of reduced graphene oxide with nitrogen and its effect on the quenching of the material's photoluminescence, Carbon. 50 (2012) 5286–5291.
[68] R. Muzyka, et al., Characterization of graphite oxide and reduced graphene oxide obtained from different graphite precursors and oxidized by different methods using Raman spectroscopy, Mater. 11 (2018) (Article 1050).
[69] S.-W. Kim, et al., Studying the reduction of graphene oxide with magnetic measurements, Carbon. 142 (2019) 373–378.
[71] A. Romero, et al., Comparative study of different scalable routes to synthesize graphene oxide and reduced graphene oxide, Mater. Chem. Phys. 203 (2018) 284–292.
[72] M. Aqeel, et al., TiO2 @ RGO (reduced graphene oxide) doped nanoparticles demonstrated improved photocatalytic activity, Mater. Res. Express. 6 (2019) (Article 086215).
[73] W. Tian, et al., A review on lattice defects in graphene: types generation effects and regulation, Micromachines. 8 (2017) (Article 163).
[74] F. Banhart, et al., Structural defects in graphene, ACS Nano 5 (2011) 26–41.
[75] L.B. Mccusker, et al., Rietveld refinement guidelines, J. Appl. Crystallogr. 32 (1999) 36–50.
[76] N. Kolev, et al., Raman spectroscopy of $CaCu_3Ti_4O_{12}$, Phys. Rev. B Condens. Matter 66 (2002) 1–4.
[77] Y. Tezuka, et al., Electronic structure study of $CaCu_3Ti_4O_{12}$ by means of X-ray Raman scattering, J. Electron Spectrosc. Relat. Phenom. 220 (2017) 114–117.
[78] J.A. Cortés, et al., Dielectric and non-ohmic analysis of Sr^{2+} influences on $CaCu_3Ti_4O_{12}$-based ceramic composites, Mater. Res. Bull. 134 (2021) (Article 111071).
[79] S. Orrego, et al., Photoluminescence behavior on Sr^{2+} modified $CaCu_3Ti_4O_{12}$ based ceramics, Ceram. Int. 44 (2018) 10781–10789.
[80] M.A. Pimenta, et al., Studying disorder in graphite-based systems by Raman spectroscopy, Phys. Chem. Chem. Phys. 9 (2007) 1276–1291.
[81] L.H. Oliveira, et al., Correlation between photoluminescence and structural defects in $Ca_{1+x}Cu_{3-x}Ti_4O_{12}$ systems, J. Am. Ceram. Soc. 96 (2013) 209–217.
[82] R. Schmidt, et al., Effects of sintering temperature on the internal barrier layer capacitor (IBLC) structure in $CaCu_3Ti_4O_{12}$ (CCTO) ceramics, J. Eur. Ceram. Soc. 32 (2012) 3313–3323.
[83] J. Mohammed, et al., Lightweight SrM/CCTO-rGO nanocomposites for optoelectronics and Ku band microwave absorption, J. Mater. Sci. Mater. Electron. 30 (2019) 4026–4040.
[84] K.W. Borth, et al., Iron oxide nanoparticles obtained from steel waste recycling as a green alternative for Congo red dye fast adsorption, Appl. Surf. Sci. 546 (2021) (Article 149126).
[85] V.G. Teixeira, et al., Principais métodos de caracterização da porosidade de resinas à base de divinilbenzeno, Quim Nova 24 (2001) 808–818.
[86] K.S.W. Sing, et al., Reporting physisorption data for gas/solid systems-with special reference to the determination of surface area and porosity, Pure Appl. Chem. 57 (1985) 603–619.
[87] R. Parra, et al., Photoluminescent $CaCu_3Ti_4O_{12}$-based thin films synthesized by a sol-gel method, J. Am. Ceram. Soc. 91 (2008) 4162–4164.
[88] K. Krishnamoorthy, et al., Investigation of Raman and photoluminescence studies of reduced graphene oxide sheets, Appl. Phys. A: Mater. Sci. Proc. 106 (2012) 501–506.
[89] F. Ben Slama Sweii, et al., Effect of annealing treatment on optical and electrical properties of PCDTBT: graphene hybrid structure for photovoltaic application, J. Electron. Mater. 49 (2020) 410–418.
[90] C. Ran, et al., Study on photoluminescence quenching and photostability enhancement of MEH-PPV by reduced graphene oxide, J. Phys. Chem. C 116 (2012) 23053–23060.
[91] X.Y. Zhang, et al., Graphene/TiO_2 nanocomposites: synthesis, characterization and application in hydrogen evolution from water photocatalytic splitting, J. Mater. Chem. 20 (2010) 2801–2806.
[92] M.S.A. Sher Shah, et al., Green synthesis of biphasic TiO_2-reduced graphene oxide nanocomposites with highly enhanced photocatalytic activity, ACS Appl. Mater. Interfaces 4 (2012) 3893–3901.
[93] F. Moura, et al., Intense photoluminescence emission at room temperature in calcium copper titanate powders, Ceram. Int. 39 (2013) 3499–3506.
[94] Y.T. Li, et al., Nearly white light photoluminescence from ZnO/rGO nanocomposite prepared by a one-step hydrothermal method, J. Alloys Compd. 715 (2017) 122–128.
[95] S. Begum, et al., Review of chitosan composite as a heavy metal adsorbent: material preparation and properties, Carbohydr. Polym. 259 (2021) (Article 117613).
[96] S.N. Ahmed, W. Haider, Heterogeneous photocatalysis and its potential applications in water and wastewater treatment: a review, Nanotechnol. 29 (2018) (Article 342001).
[97] H. Yan, et al., Effects of the oxidation degree of graphene oxide on the adsorption of methylene blue, J. Hazard. Mater. 268 (2014) 191–198.
[98] L. Hou, et al., CO gas sensors based on p-type CuO nanotubes and CuO nanocubes: morphology and surface structure effects on the sensing performance, Talanta. 188 (2018) 41–49.
[99] U. Coleto Jr., et al., An approach for photodegradation mechanism at TiO_2/$SrTiO_3$ interface, J. Mater. Sci. Mater. Electron. 29 (2018) 20229–20329.
[100] S. Sumikura, et al., Photoelectrochemical characteristics of cells with dyed and undyed nanoporous p-type semiconductor CuO electrodes, J. Photochem. Photob. A: Chem. 194 (2008) 143–147.
[101] Y.K. Jeong, G.M. Choi, Nonstoichiometry and electrical conduction of CuO, J. Phys. Chem. Solids 57 (1996) 81–84.
[102] J.Q. Jiang, et al., Preliminary study of ciprofloxacin (cip) removal by potassium ferrate (VI), Sep. Purif. Technol. 88 (2012) 95–98.
[103] H.S. Kushwaha, et al., Efficient solar energy conversion using $CaCu_3Ti_4O_{12}$ Photoanode for Photocatalysis and Photoelectrocatalysis, Sci. Rep. 6 (2015) (Article 18557).